UC Santa Cruz

UC Santa Cruz Previously Published Works

Title

Auto-acoustic compaction in steady shear flows: experimental evidence for the suppression of shear dilatancy by internal acoustic vibration

Permalink

https://escholarship.org/uc/item/2878x3q1

Authors

Van der Elst, Nicholas J
Brodsky, Emily E
Le Bas, Pierre-Yves
et al.

Publication Date

2012-09-28

Peer reviewed

eScholarship.org Powered by the California Digital Library
University of California

Auto-acoustic compaction in steady shear flows: Experimental evidence for suppression of shear dilatancy by internal acoustic vibration

Nicholas J. van der Elst,[1] Emily E. Brodsky,[1] Pierre-Yves Le Bas,[2] and Paul A. Johnson[2]

Received 22 September 2011; revised 9 August 2012; accepted 20 August 2012; published 28 September 2012.

[1] Granular shear flows are intrinsic to many geophysical processes, ranging from landslides and debris flows to earthquake rupture on gouge-filled faults. The rheology of a granular flow depends strongly on the boundary conditions and shear rate. Earthquake rupture involves a transition from quasi-static to rapid shear rates. Understanding the processes controlling the transitional rheology is potentially crucial for understanding the rupture process and the coseismic strength of faults. Here we explore the transition experimentally using a commercial torsional rheometer. We measure the thickness of a steady shear flow at velocities between 10^{-3} and 10^{2} cm/s, at very low normal stress (7 kPa), and observe that thickness is reduced at intermediate velocities (0.1–10 cm/s) for angular particles, but not for smooth glass beads. The maximum reduction in thickness is on the order of 10% of the active shear zone thickness, and scales with the amplitude of shear-generated acoustic vibration. By examining the response to externally applied vibration, we show that the thinning reflects a feedback between internally generated acoustic vibration and granular rheology. We link this phenomenon to acoustic compaction of a dilated granular medium, and formulate an empirical model for the steady state thickness of a shear-zone in which shear-induced dilatation is balanced by a newly identified mechanism we call auto-acoustic compaction. This mechanism is activated when the acoustic pressure is on the order of the confining pressure, and results in a velocity-weakening granular flow regime at shear rates four orders of magnitude below those previously associated with the transition out of quasi-static granular flow. Although the micromechanics of granular deformation may change with greater normal stress, auto-acoustic compaction should influence the rheology of angular fault gouge at higher stresses, as long as the gouge has nonzero porosity during shear.

Citation: van der Elst, N. J., E. E. Brodsky, P.-Y. Le Bas, and P. A. Johnson (2012), Auto-acoustic compaction in steady shear flows: Experimental evidence for suppression of shear dilatancy by internal acoustic vibration, *J. Geophys. Res.*, *117*, B09314, doi:10.1029/2011JB008897.

1. Introduction

[2] Frictional sliding processes in geophysics often involve granular shear flows at the sliding interface. This is true for landslides and debris flows, as well as for earthquake ruptures within granulated damage zones or gouge-filled faults. The frictional strength in these contexts is controlled by the rheology of the granular flow, which has a strong dependence on shear rate and boundary conditions [*Campbell*, 2006; *Clement*, 1999; *Iverson*, 1997; *Savage*, 1984].

[3] For different shear rates, confining stresses, and packing densities, the description of a granular flow can range from "solid-like" to "gas-like" [*Jaeger et al.*, 1996], albeit with complicated second-order behavior in each regime. The appropriate description for a particular flow is typically determined by the dimensionless inertial number, which compares the magnitude of the grain inertial stresses to the confining stress [*Bocquet et al.*, 2001; *Campbell*, 2006; *Clement*, 1999; *Iverson*, 1997; *Lu et al.*, 2007; *Savage*, 1984]

$$I \equiv \frac{\rho d \dot{\gamma}^2}{p}, \tag{1}$$

where ρ is density, d is grain diameter, $\dot{\gamma}$ is the strain rate, and p is the confining (normal) pressure. The shear rate profile in boundary driven flows is commonly observed to decay

[1]Department of Earth and Planetary Science, Univ. of California, Santa Cruz, California, USA.
[2]Geophysics Group, Los Alamos National Laboratory, Los Alamos, New Mexico, USA.

Corresponding author: Nicholas J. van der Elst, Department of Earth and Planetary Science, 1156 High St., Univ. of California, Santa Cruz, CA 95060, USA. (nvandere@ucsc.edu)

©2012. American Geophysical Union. All Rights Reserved.
0148-0227/12/2011JB008897

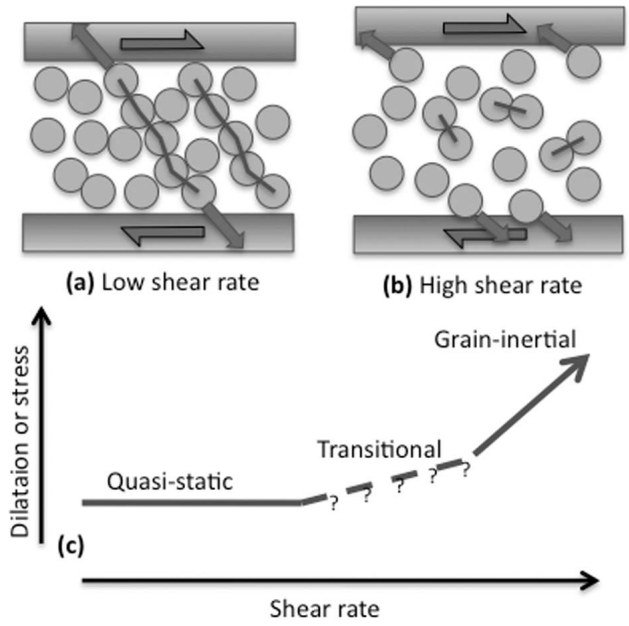

Figure 1. Cartoon depiction of end-member granular flow regimes. (a) In the low shear rate quasi-static regime, boundary stresses are supported elastically through force chains. Thin lines represent grain-grain contacts and arrows represent forces acting on the boundaries. (b) In the high shear-rate grain-inertial regime, stresses are supported through momentum transfer in collisions. (c) Cartoon of experimental behavior in end-member regimes. The y axis represents stress under constant volume conditions or shear zone thickness under constant stress conditions. In the quasi-static regime, shear dilatation and stress are independent of shear rate, resulting in a friction-like rheology. In the grain inertial regime, dilatation and stress are proportional to the momentum transfer rate, resulting in a power law viscous-like rheology. This study focuses on the intermediate shear rate transitional regime, where stresses are supported elastically, but vibration becomes important for force chain stability.

approximately exponentially [*Bocquet et al.*, 2001; *Veje et al.*, 1999] (Appendix A), such that $\dot{\gamma} \sim v/d$ where v is the boundary velocity, and equation (1) simplifies to

$$I = \frac{\rho v^2}{p}. \tag{2}$$

In the solid-like or quasi-static regime ($I \ll 1$), forces are transmitted elastically through a network of grain contacts, called force chains, and the shear and normal stresses at the boundaries are related to the stiffness and orientations of these chains (Figure 1a) [*Majmudar and Behringer*, 2005]. In this regime, force chains are continually created and destroyed through shearing, but the rate of buckling and destruction of old force chains is equal to the rate of creation of new ones, and the shear resistance is, to first order, independent of the shear rate (Figure 1c). This results in a solid-like frictional rheology. In the gas-like, inertial flow regime ($I \gg 1$), stresses are supported through grain-grain or grain-boundary collisions, analogous to a kinetic gas model (Figure 1b). The shear and normal stresses are then related to the particle momentum transfer rate, resulting in a power law viscous-like rheology (Figure 1c) [*Bagnold*, 1954; *Campbell*, 2005].

[4] Earthquake rupture and debris flows likely involve a transition between quasi-static and rapid inertial shear, in which vibration and momentum become important for the rheology of the flow. A description of granular rheology in this transitional regime is therefore required for a full understanding of the process of rupture nucleation and propagation. However, our understanding of the rheology of dense, rapid granular flows ($I \sim 1$) is far from complete.

[5] Some of the difficulty in describing the rheology of a dense, rapid granular flow arises from the athermal nature of the granular medium. Unlike a traditional gas or liquid, a granular material does not explore particle configurations and approach an equilibrium state in the absence of an external energy source [*Jaeger et al.*, 1996]. Consequently, the rheology of a granular medium depends strongly on the detailed configuration of grains. Under the same pressure or volume conditions, some grain (packing) configurations can be very stiff, while others may be soft or 'fluidized.' A striking example of this dependency on grain configuration is the phenomenon of jamming/unjamming [*Liu and Nagel*, 2010] where a granular medium transitions dramatically from a solid-like to a fluid-like phase, or vice versa, under small perturbations to particle configuration or loading direction [*Aharonov and Sparks*, 1999; *Cates et al.*, 1998; *Liu and Nagel*, 1998].

[6] A good way to un-jam a granular material is to add vibration. This provides an external energy source that allows a granular system to explore packing configurations. Vibration usually leads to a more compact configuration, depending on the initial packing density and the amplitude of the vibration [*Knight et al.*, 1995; *Nowak et al.*, 1997]. Another source of external energy is imposed shear. Under shear, a granular medium may dilate or compact, depending on its starting configuration. Starting from a dense state, such as random (or ordered) close packing, it must dilate in order to allow geometrically frustrated grains to move past each other (i.e., un-jam) [*Lu et al.*, 2007; *Marone*, 1991; *Reynolds*, 1885]. Acoustic vibration and imposed shear are thus two sources of external energy that tend to drive the packing density of a granular system in opposite directions.

[7] For gouge-filled faults, both acoustic and shear energy sources are present, with acoustic energy generated during rupture, or arriving in seismic waves from nearby earthquakes. In granular shear experiments, bursts of acoustic vibration can trigger compaction and stick–slip events and generate lasting changes in rheology [*Johnson et al.*, 2008, 2012]. In other experiments, vibration has caused a transition from a disordered to a crystallized (perfectly ordered) state when the kinetic energy of vibration balances that of shearing [*Daniels and Behringer*, 2005]. Acoustic fluidization, in which scattered wave energy produces transient reductions in fault normal stress, has been proposed as a mechanism for reducing shear resistance during earthquake slip [*Melosh*, 1996].

[8] Here we experimentally explore the behavior of a sheared granular medium when the shearing itself generates acoustic vibration. Our starting point is a recent experiment that showed that the thickness of a steady, shear-driven flow

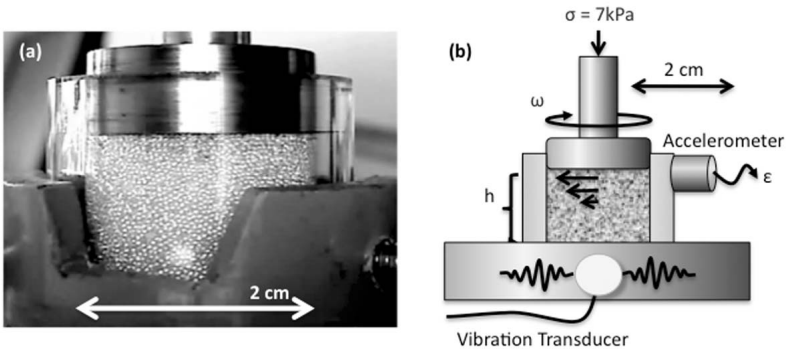

Figure 2. Experimental apparatus: TA Instruments AR2000ex torsional rheometer, with parallel plate geometry. (a) Photograph of test chamber in mounting bracket. The 2 cm quartz jacket is here filled with glass beads. (b) Schematic of the experimental geometry. Shear rate ω and normal stress σ are controlled through the upper rotor. The normal stress σ is held constant at 7 kPa by adjusting the rotor height h. We also measure, but do not report on, the torque τ (i.e., shear stress) required to shear at a given velocity.

is non-monotonic with respect to shear velocity [*Lu et al.*, 2007]. At velocities intermediate between quasi-static and grain-inertial flow (the transitional regime, Figure 1c), steady state thickness of the shear zone is markedly reduced. Under constant volume conditions, this thinning manifests as a drop in shear strength and normal pressure. This behavior is not anticipated by theoretical treatments of granular flow, which predict monotonic dilation with shear rate [*Bagnold*, 1954; *Campbell*, 1990, 2006; *Clement*, 1999] nor by experiments carried out at lower shear rates and higher pressures [*Marone et al.*, 1990; *Marone*, 1991]. Numerical experiments using idealized particles also fail to anticipate this transitional compaction [*da Cruz et al.*, 2005; *GDR MiDi*, 2004]. The non-monotonic behavior at intermediate shear rates has recently been confirmed in several independent experiments [*Dijksman et al.*, 2011; *Kuwano and Takahiro*, 2011]. This phenomenon is much more pronounced for highly angular particles than for smooth particles.

[9] We propose in this paper that the intermediate shear-rate thinning observed in prior experiments can be explained as auto-acoustic compaction; at moderate shear rates, grain interactions generate acoustic vibration that causes compaction and suppression of shear-induced dilatation. The tradeoff between shear dilatation and shear-induced acoustic compaction results in a shear-rate dependent steady state thickness of the shear zone. The competition between vibrational compaction and shear dilation we propose is reminiscent of the crystallization/melting transition described by *Daniels and Behringer* [2005], in which vibration is interpreted to weaken force chains and reduce the internal granular pressure.

[10] To resolve this problem, we first reproduce the observations of *Lu et al.* [2007], measuring the steady state thickness of a sheared granular medium over a range of shear rates. We record the amplitude of acoustic emissions produced during shear, and then apply similar amplitudes of acoustic vibration using an external vibration transducer and observe the effect on steady state shear zone thickness. We also perform experiments in which we subject the shear zone to either transient acoustic pulses or transient shear-rate steps. We find that external acoustic vibration reduces the steady state thickness of the shear zone in the same way as shear-generated vibration. Using the time-dependent evolution of shear dilatation and acoustic compaction, we then formulate a quantitative model for steady state layer thickness. The experiments are performed at low normal stress (7 kPa), so as a last step we develop a scaling law for predicting behavior at higher stresses.

2. Methods

[11] In this section we introduce the experimental apparatus, discuss the boundary conditions and normal force control, and describe the acoustic monitoring and external vibration setup. We also describe the granular media, and introduce the basic types of experiment to be performed. The experimental procedures will be described in more detail in Section 3 as we go through the results.

2.1. Experimental Apparatus

[12] The experimental apparatus is a TA Instruments AR2000ex commercial torsional rheometer with rotating parallel plate geometry (Figure 2). This instrument is capable of sensitive measurement and control of torque, angular velocity, and layer thickness, and covers a large range of velocities ($\sim 10^{-5}$ to 300 rad/s), but is limited in the magnitude of the applied forces (50 N normal force, 0.2 N-m torque). This is nearly identical to the instrument used in *Lu et al.* [2007] and *Kuwano and Takahiro* [2011].

[13] Torque, sample thickness, normal force, shear rate, and displacement are all measured by the rheometer electronics. Torque is measured to within 1 nN-m through the current required to drive the rheometer magnetic drag cup. Angular displacement is measured to within 40 nRad by an optical encoder on the rheometer spindle. Rotor height (sample thickness) is controlled by a ball slide screw and measured to within 0.1 μm by an optical encoder on the screw motor. Normal force is measured to 1 mN by a force transducer in the base of the sample mount. The maximum sampling rate permitted by the AR Instrument Control data logger is 1 Hz. The experiments are conducted at room temperature and humidity in a climate-controlled lab.

[14] The granular sample is housed in a quartz glass cylindrical jacket with dimensions 19 mm diameter by

15 mm height (Figure 2). A layer of particles is epoxied to the base of the chamber and to the upper rotor, to force internal shear rather than slip at the boundaries. The quartz cylinder is filled only to 10–14 mm depth, so that the rotor plate is jacketed as well. Friction between the rotor and the quartz jacket is minimized by carefully centering the sample. The residual torque is typically 50–300 μNm, or 0.6–3% of the average total torque during sample deformation. While a study of the normal and shear stresses would require a correction for jacket friction, we are primarily interested in the steady state sample thickness, and the residual friction between the rotor and jacket is relatively unimportant.

2.2. Controlled Stress Boundary Conditions and Relation to Controlled Volume

[15] All experiments are carried out under controlled normal stress conditions (7 kPa). This low normal stress minimizes grain fracture and emphasizes the effect of grain interlocking, rolling, and sliding in shear deformation. The possible limitations of using such a low normal stress are taken up in the discussion at the end of the paper.

[16] Normal stress is maintained by the rheometer controller software through adjustment of the sample thickness. The normal stress control has a somewhat slow feedback timescale, however, resulting in normal stress fluctuations in response to sudden dilation or compaction (Appendix B). Furthermore, the controller software only adjusts sample thickness in response to normal force fluctuations exceeding 10% of the target value. These two features tend to damp out small, rapid fluctuations, which is desirable in some applications, but introduces two difficulties for this study. 1) The finite time response makes it difficult to interpret the intrinsic time scale for sample compaction in response to a sudden acoustic or shear-rate pulse (Appendix B). 2) The 10% minimum fluctuation results in an apparent hysteresis in thickness between ascending and descending velocity ramps that actually reflects a hysteresis in the average imposed normal stress. These two caveats must be kept in mind when interpreting the second-order features of the data presented in this study.

[17] We employ constant normal stress rather than constant volume boundary conditions because the large variations in shear zone thickness would otherwise result in either decoupling of the sample during compaction phases, or locking up of the mechanical drive during dilatation. However, qualitatively similar results are obtained when measuring the evolution of normal stress under constant volume conditions [*Lu et al.*, 2007, 2008].

[18] Following the argument of *Lu et al.* [2007], the correspondence between normal stress and layer thickness for alternate boundary conditions is a consequence of the cyclic rule, which states the relationship between the partial derivatives of a three-variable constitutive law

$$\left(\frac{\partial V}{\partial \dot{\gamma}}\right)_{\sigma} = -\left(\frac{\partial V}{\partial \sigma}\right)_{\dot{\gamma}} \left(\frac{\partial \sigma}{\partial \dot{\gamma}}\right)_{V}. \tag{3}$$

The change in volume V (or layer thickness) with shear rate $\dot{\gamma}$ at constant load is related to the change in stress σ with shear rate at constant volume through the compressibility term $(\partial V/\partial \sigma)_{\dot{\gamma}}$. The compressibility term may be quite complicated for a granular flow [*Daniels and Behringer*, 2005], but assuming it exists and is negative, layer compaction under constant load implies normal stress reduction under constant volume.

2.3. Acoustic Vibration

[19] External acoustic vibration is produced by a ceramic transducer (PZT-5) affixed to the base plate of the rheometer adjacent to the sample chamber. An accelerometer (Bruel and Kjaer 4373 charge accelerometer), attached directly to the cylindrical jacket outside the active shear zone, measures the acoustic vibration intensity. In order to achieve high acoustic strain amplitude with a small source transducer, we vibrate at the resonant frequency of the mechanical system, i.e., the frequency that produces the largest measured peak amplitudes in the accelerometer, which is found to be 40.2 kHz. Note that this is the natural frequency of the entire apparatus, not necessarily the sample chamber itself, which has a fundamental frequency between 28 and 34 kHz based on the acoustic wave speed found below.

[20] We measure peak acceleration, but express acoustic intensity in terms of peak strain. Peak acceleration is measured over 1-s intervals, and then averaged over the duration of each 20-s velocity step. Peak acoustic strain ε is then estimated by dividing the peak acceleration a by the dominant frequency of the vibration (f = 40.2 kHz) to get particle velocity, and then dividing by the acoustic wave speed c

$$\varepsilon \approx \frac{a}{2\pi f c} \approx \frac{v}{c}. \tag{4}$$

We are unable to directly measure acoustic travel time to calculate c. We instead measure the shear modulus of the aggregate and use an assumed range of effective Poisson's ratios to calculate a rough estimate of c, using the equation

$$c = \sqrt{\frac{2G(1-\nu)}{\rho(1-2\nu)}}, \tag{5}$$

where ρ is the density, G is the shear modulus, and ν is the Poisson's ratio of the aggregate. This equation is defined for an elastic solid, and is only approximately valid for a granular aggregate in the long-wavelength limit [*Walton*, 1987; *Makse et al.*, 2004]. The shear modulus of our aggregate sample is 1.1×10^8 Pa, as measured by an oscillatory strain test with frequency 100 Hz. The aggregate density is 1500 kg/m^3. Assuming a Poisson's ratio between 0 and 0.25, this gives an acoustic wave speed c between 390 and 480 m/s. By using the range of possible Poisson's ratios to place a bound on the wave speed, we are assuming that the bulk modulus and shear modulus in an aggregate material are related through the Poisson's ratio – a questionable assertion for a granular medium. However, the calculated wave speed agrees well with other experiments on acoustic travel time in granular media, extrapolated to slightly lower pressures [*Coghill and Giang*, 2011; *Jia et al.*, 1999], as well as with theoretical predictions using effective medium theory and elastic properties of the individual grains [*Makse et al.*, 2004; *Walton*, 1987].

[21] The acoustic vibration frequency (40.2 Hz) is therefore slightly higher than the natural frequency of the sample (~30 kHz), but much lower than the natural frequency of a single grain (~MHz). The accelerometer has a flat response

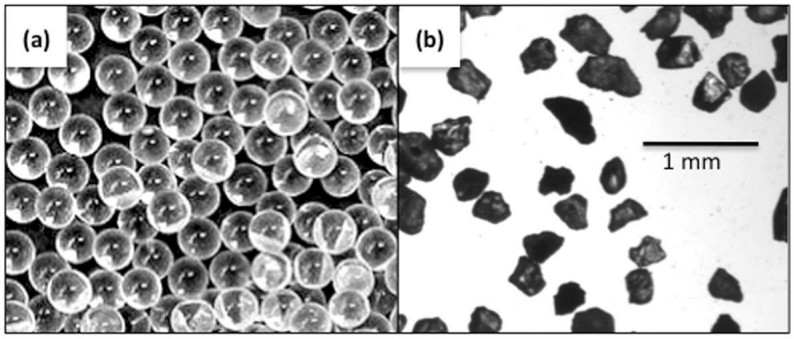

Figure 3. Granular media used in experiments: (a) smooth soda-lime glass beads, (b) angular Santa Cruz beach sand.

up to 35 kHz and detailed analysis of the shear-generated acoustic spectrum and the frequency dependence of the rheological response are beyond the scope of this study. We note, however, that recent preliminary tests using a more powerful amplifier to generate equivalent strains with lower frequencies (down to 1 kHz) show qualitatively similar results.

2.4. Granular Media

[22] We test two different granular materials with different grain shapes (Figure 3), but equivalent sizes and densities: spherical glass beads (soda-lime glass sandblasting beads, (mono-disperse, mean diameter: 350 μm) and angular beach sand (from Cowell's Beach in Santa Cruz) (range: 250–500 μm, uniformly distributed; mean: 350 μm). The beach sand is chosen for its high angularity and high fracture resistance. The composition of the sand is roughly 44% quartz, 37% lithics, and 19% feldspars [*Paull et al.*, 2005]. The composition of the heavy minerals and lithic fragments is detailed by *Hutton* [1959].

2.5. Experimental Procedures

2.5.1. Velocity Ramps

[23] The primary experiment consists of a suite of angular velocity ramps between 10^{-3} to 100 rad/s (9.5×10^{-4} to 95 cm/s at the outer rim of the rotor) under controlled normal stress, in which we report sample thickness (Section 3.1, 3.3). The velocity is incremented gradually from slow to fast and fast to slow, multiple times per sample. The repeated velocity ramps extend the work of *Lu et al.* [2007], who focused mostly on a single velocity ramp per sample. Each velocity step lasts 20 s, and the reported thickness is averaged over the last 10 s of each step. The duration of the steps is chosen to allow the shear zone to evolve to a new steady state thickness value after each small step in velocity. We refer to these thickness observations as steady state, in that they do not depend on the direction of the velocity ramp or the duration of the observation. Throughout this paper, we refer to this experimental procedure as a velocity ramp, although in reality it consists of small discrete velocity steps. The velocity ramp experiments are summarized in Table 1.

[24] We first run the velocity ramps in the absence of acoustic vibration to establish the baseline, steady state thickness of the shear zone as a function of shear rate. During these experiments, we record the shear-rate dependent amplitude of acoustic vibration produced internally by grain interactions. We then perform velocity ramps in the presence of constant amplitude external vibration and examine the effect on steady state thickness.

2.5.2. Acoustic Pulses and Shear-Rate Pulses

[25] In the second type of experiment, we subject the sample either to acoustic pulses or transient shear-rate steps (Sections 3.6, 3.7). In the acoustic pulse experiments, we shear the sample at a slow, constant rate of 0.01 rad/s to minimize internally generated vibration and shear dilatation, and then introduce 60-s pulses of acoustic vibration at various amplitudes. In the shear-rate pulse experiments, the sample is sheared at a constant rate of 0.1 rad/s, and then subjected to 60-s jumps in shear rate. The higher baseline shear rate is chosen to minimize the transient effects of the shear-rate jump. The pulse experiments are summarized in Table 2.

Table 1. Velocity Ramp Experiments

Name	Material	Number Without Vibration[a]	Number With Vibration[a]	Correction[b]
VRS1	Sand	4 (2,2)	8 (4,4)	yes
VRS2	Sand	2 (1,1)	8 (4,4)	No
VRS3[c]	Sand	10 (5,5)	6 (3,3)	No
VRS4	Sand	0	8 (4,4)	No
VRG1	Glass beads	17 (9,8)	6 (3,3)	No

[a](N,M) signifies N slow-to-fast and M fast-to-slow velocity ramps, respectively.
[b]Linear correction for run-in phase applied to runs without vibration.
[c]Shown in Figure 7.

Table 2. Pulse Experiments (Sand)

Name	Pulse Type	Starting Shear Rate	Pulse Shear Rate (rad/s)	Acoustic Strain	b^a (μm)	Runs
SPS1	Shear	0.1	1.0	1.3×10^{-5}	1.9 ± 1.9	10
		0.1	2.0	2.2×10^{-5}	5.6 ± 2.7	5
		0.1	3.16	2.9×10^{-5}	10.5 ± 0.6	5
		0.1	5.0	3.5×10^{-5}	14.2 ± 1.2	5
APS1	Acoustic	0.01	n/a	1.3×10^{-6}	0.9 ± 4.6	13
		0.01		3.8×10^{-6}	2.7 ± 3.0	10
		0.01		1.4×10^{-5}	0.1 ± 3.3	5
		0.01		2.4×10^{-5}	8.6 ± 3.6	5
		0.01		3.0×10^{-5}	9.1 ± 3.3	6

[a]Compaction magnitude (equation (6)) with τ^- held constant at 10 s for all curves.

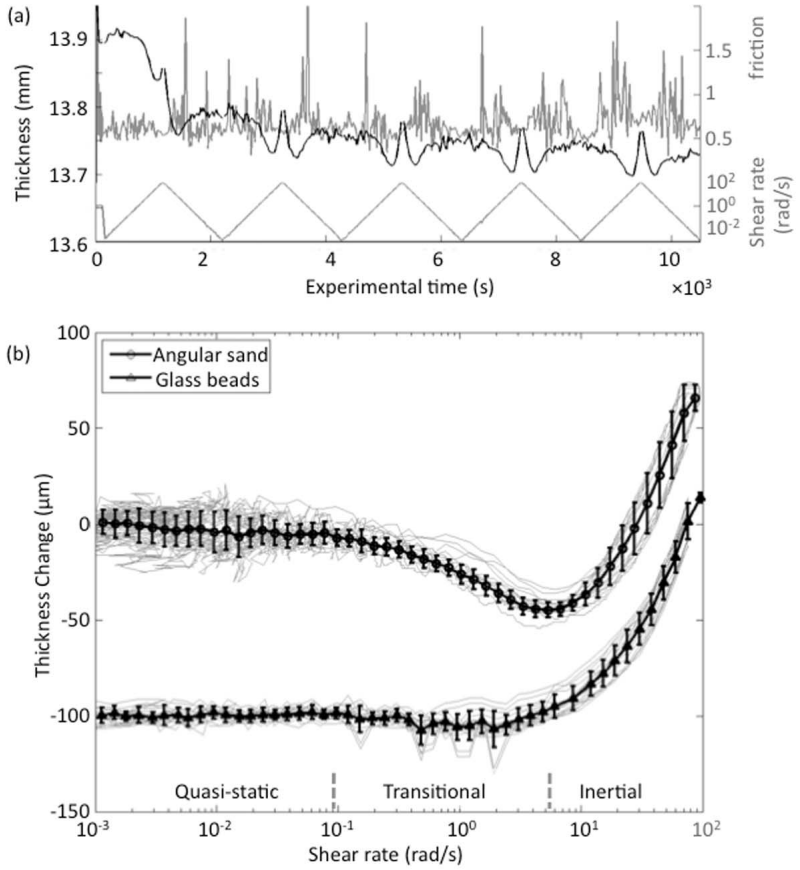

Figure 4. (a) Thickness versus experimental time for the run-in phase of the experiment with angular sand. Sample thickness decreases logarithmically with displacement, with the shear-rate dependent reversible thickness component (b) superimposed. Friction shows strong fluctuations, particularly at intermediate shear rates. (b) Steady state thickness versus shear rate for angular sand and glass beads. Individual curves represent multiple upgoing and downgoing velocity ramps (Table 1), and thick error bars show means and standard deviations between runs. Thickness is independent of shear rate at low shear rates, and strongly dependent on shear rate for intermediate and high shear rates. Compaction is observed at intermediate shear rates for angular sand, but not for smooth glass beads. Thickness is reported relative to starting thickness, offset by 100 microns for the glass beads.

[26] The amplitude of the shear-induced acoustic vibration is captured by the accelerometer, allowing us to compare the magnitude of compaction under equivalent-amplitude external and shear-induced vibration. We use the information gained from the pulse experiments to explain the steady state thickness variations in the velocity ramp experiments in Section 4.

3. Results

3.1. Velocity Ramps–Shear Induced Dilatation and Compaction

[27] The velocity ramp produces two effects: 1) long-term compaction of the granular sample that goes with total displacement, and 2) reversible and repeatable shear-rate dependent fluctuations about this long-term compaction trend (Figure 4a). The long-term trend is irreversible and diminishes with the logarithm of displacement. This irreversible compaction is interpreted as compaction in the non-shearing bulk of the granular sample [*Chambon et al.*, 2006]. The reversible shear-rate dependent features, on the other hand, do not diminish in amplitude with displacement. In the following, we focus almost exclusively on describing the reversible and repeatable component of compaction, which we interpret as reflecting thickness changes in the actively shearing layer (see Appendix A for a definition of the actively shearing layer). We typically report the velocity ramp data only after the irreversible long-term compaction is complete, treating the first $\sim 10^4$ radians displacement as a prolonged 'run-in' phase, but in one case we resort to making a correction for the tail end of the run-in phase (noted in Table 1).

[28] The reversible variation of sample thickness with shear rate is shown in Figure 4b. The velocity ramp curves in this figure are taken from several experiments using separately prepared samples, after $\sim 10^4$ radians run-in displacement (Table 1). Both angular sand and smooth glass beads deform with a thickness that is independent of shear-rate at very low shear rates (10^{-3}–10^{-1} rad/s), and show strong dilation at very high shear rates (>10 rad/s). However, the

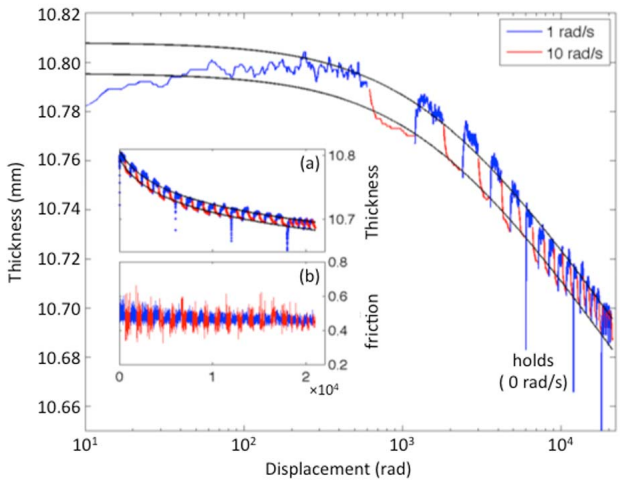

Figure 5. Long-displacement steady shear experiment with alternating shear rates (1 and 10 rad/s). Displacement starts from 10 radians to show both the irreversible and reversible components of compaction in the transitional regime. Solid lines are a logarithmic fit to the irreversible component. Three holds in which shear rate and shear stress are set to zero for 60 s produce pronounced drops in thickness that are then recovered during renewed shear. Inset (a) gives the same data on a linear scale, from 0 radians. Inset (b) gives the evolution of friction. Velocity weakening behavior disappears with increasing displacement.

behavior of the two granular media differs greatly at intermediate shear rates (0.1–7 rad/s), where the thickness of the angular sand decreases markedly. The glass beads show only a hint of this thinning at intermediate shear-rates. The sample thickness follows the same path with respect to shear rate, regardless of whether the shear rate is increasing or decreasing, although there is a slight hysteresis at high shear rates, which we attribute to the normal force control algorithm (see Section 2.2).

[29] The behavior of the granular media at either end of the velocity range can be understood in terms of the end-members of granular flow (equation (2), Figure 1). The glass beads show a relatively monotonic transition between the flow regimes, with constant thickness in the quasi-static regime and dilation in the grain inertial regime (Figure 4). Dilation begins at shear rates above ∼30 rad/s (cm/s), corresponding to a dispersive pressure ∼200 Pa, which is about 3% of the normal pressure p = 7 kPa (equation (2)). Consequently, we never fully reach the inertial regime where stress and thickness should scale as the square of shear rate [*Bagnold*, 1954].

[30] The behavior of the angular sand at intermediate share rates, however, is more complex than anticipated by either end-member granular flow regime. At intermediate shear rates there is a robust reversible reduction in steady state layer thickness, reproducing the findings of *Lu et al.* [2007]. This transitional compaction, on the order of 50 μm at maximum, occurs regardless of the direction of the velocity ramp. The active shear zone thickness is on the order of a few grains, with a scale depth of ∼600 μm (Appendix A), putting the maximum compaction at ∼10% of the shear zone thickness. This transitional behavior has recently been confirmed in independent experiments [*Dijksman et al.*, 2011; *Kuwano and Takahiro*, 2011], but a physical understanding of the transitional regime has yet to be developed.

3.2. Probing Reversible and Irreversible Compaction at Alternating Shear Rates

[31] To more clearly demonstrate the relationship between the reversible, shear-rate dependent component and the irreversible run-in phase (Figure 4a), we run an additional experiment using alternating shear rates rather than a continuous velocity ramp. (Note that we have not yet arrived at the shear-rate pulse experiments described in Section 2.5.2.) Starting from zero displacement we impose steady shear, alternating between 1 and 10 rad/s at intervals of 600 radians (Figure 5). These shear rates are well within the transitional shear thinning regime. The difference in steady state thickness between these two shear rates in the velocity ramp is 12.5 μm (Figure 4).

[32] Viewed over the long-term, both shear rates produce logarithmic compaction at a rate that is proportional to shear rate, and hence scales with displacement (Figure 5). Increases in shear rate produce decreases in thickness that are superimposed on the irreversible long-term trend. The reversible thickness difference is 12.5 μm, exactly consistent with the velocity ramp experiments (Figure 4). This shear-rate dependent thickness change does not decrease in amplitude as the irreversible component diminishes, again consistent with the velocity ramps.

[33] Also shown in Figure 5 are three relaxation holds in which the shear rate and torque were set to zero for 60 s. These relaxation holds result in ∼0.5 mm of immediate compaction that is rapidly recovered upon resumption of shear over a displacement scale of a fraction of a radian. The 1–10 rad/s shear-rate steps, on the other hand, evolve over 10 s of radians. This highlights that a sheared medium must dilate relative to static packing, and shows that the subsequent evolution of shear-rate dependent thickness likely involves a reorganization of grains over a displacement scale somewhat larger than for the initial formation and rotation of force chains.

[34] Friction shows weak shear-rate dependence for small cumulative displacement, but this dependence disappears as displacement increases (Figure 5, inset b). Shear-rate independence of friction and thickness may be considered unusual compared to high-stress, low shear rate experiments carried out on crushed granite, in which velocity strengthening and shear-rate dependent dilatation are typically observed [e.g., *Beeler et al.*, 1996; *Biegel et al.*, 1989; *Marone et al.*, 1990]. The difference in thickness behavior may arise from the difference in micromechanics of granular deformation at low confining stress and high porosity, in which shear stresses are supported more through granular interlocking than inter-granular or boundary surface friction. On the other hand, we note that some studies show that the velocity dependence of friction in granular materials diminishes or disappears after significant cumulative displacement (hundreds of mm) [*Beeler et al.*, 1996].

[35] The thickness evolution under alternating steady shear rates (Figure 5) is entirely consistent with the behavior in the velocity ramp experiments, demonstrating that the transitional "dip" in thickness as a function of shear rate (Figure 4)

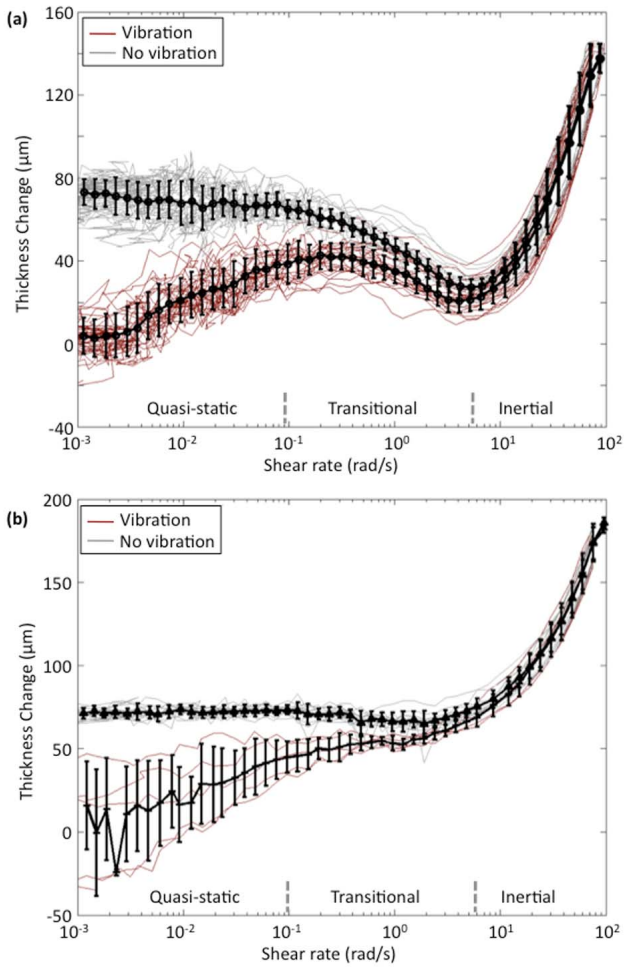

Figure 6. Steady state layer thickness as a function of shear rate for (a) angular sand and (b) smooth glass beads. Layer thickness is given relative to the minimum layer thickness under acoustic vibration. Thin lines are individual runs (Table 1); thick lines are averages over all runs. In the presence of acoustic vibration, the layer thickness is reduced and is dependent on shear rate over the entire range. The intermediate shear rate behavior is not strongly affected by the vibration.

reflects a change in the steady state thickness of the shear zone, and is not an artifact of the velocity ramp itself.

3.3. Velocity Ramps With Acoustic Vibration

[36] In the introduction, we proposed a link between shear-induced vibration and the rheology in the transitional regime. To explore the effect of shear-induced vibration on the reversible compaction observed in section 3.1, we now repeat the velocity ramps in the presence of external vibration (Figure 6). The introduction of acoustic vibration has two effects. First, it causes irreversible compaction that decays linearly with log time from the start of the vibration (Figure 7), similar to the irreversible compaction during the run-in phase (Figure 4a), which we discuss below. More importantly, it induces a strong shear-rate dependence in the reversible component at low shear rates that was not seen in the previous experiment (Figure 6). At low shear rates, the layer thickness is significantly reduced compared to the non-vibrated case. This effect is seen for the angular sand as well as for the glass beads. The reduced thickness is again a steady state value, and is reproducible regardless of whether the velocity ramp is increasing or decreasing. The steady state thickness has a positive slope with shear rate, up to the transitional regime for angular sand. At higher shear rates, there is negligible difference between the experiments with and without external acoustic vibration.

[37] A representative acoustic experiment (VRS3, Table 1) is shown as a function of experimental time in Figure 7, similar to Figure 4a. (Note, however, that the data in Figure 7 are post run-in, as opposed to in Figure 4a.) The angular sand sample is first sheared through several velocity ramps without vibration to establish the baseline shear-rate dependent behavior (Figure 7). The non-monotonic pattern of thickness versus shear rate is traced and then retraced in reverse as velocity is varied over experimental time (c.f. Figure 6a). After two complete velocity ramp cycles, the external acoustic vibration is switched on and the sample is run through several more velocity ramp cycles. During the first few cycles with vibration, irreversible compaction occurs, decreasing logarithmically in time (modeled by the thick black line). The new shear-rate dependent thickness variation at low shear rates is superimposed on this irreversible compaction component, and does not change in amplitude from cycle to cycle as the irreversible compaction runs its course. Finally, vibration is switched off and the sample recovers back to its original thickness versus shear-rate behavior, albeit at a reduced total sample thickness.

3.4. Linking Compaction and Acoustic Vibration

[38] Acoustic emissions are continuously produced during shear by sliding, jostling, and force chain buckling. There may be occasional fracturing at grain corners, although no visible quantity of fines is observed post-experiment. The accelerometer monitors these acoustic emissions, as well as the amplitude of the vibration produced by the external transducer. The observed vibration links the compaction of the angular sand in the transitional regime and the compaction achieved by external acoustic vibration (Figure 8). First, the beginning of the transitional regime for angular sand corresponds to the shear rate at which internally produced acoustic vibration becomes detectable. The vibration amplitude for glass beads is smaller at this shear rate, consistent with the much smaller transitional compaction (Figure 6). Second, at high shear rates, the internally generated vibration overwhelms the external vibration such that there is no difference in the recorded vibration amplitude with or without external vibration (Figure 8). This corresponds to the joining of the thickness versus velocity curves from the two velocity ramp experiments at ~7 rad/s (Figure 6). These observations suggest that acoustic vibration produces compaction in a similar way regardless of whether the vibration is externally or internally generated.

[39] The rollover in acoustic amplitude observed at higher shear rates (Figure 8) is due to the fact that the recorded peak amplitude begins to clip at higher shear rates. To get a more robust estimate of the scaling of vibration amplitude with shear rate, we also compute the signal power of the shear-induced vibration signal for angular sand (Figure 8 inset). Power is computed by integrating periodograms over a

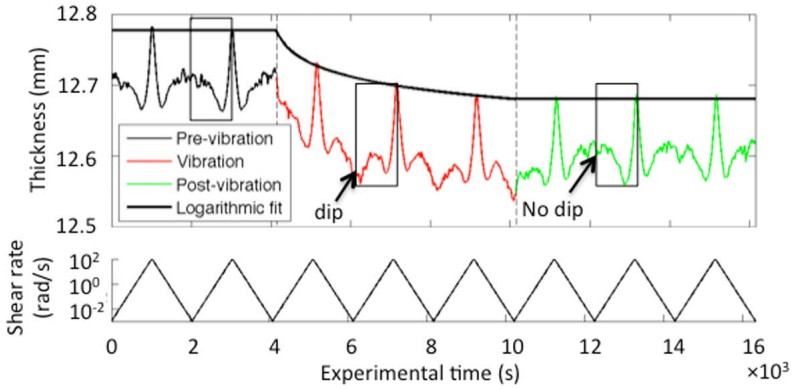

Figure 7. (top) Sample thickness and shear rate as a function of experimental time, for angular sand, showing evolution of thickness during external vibration (Experiment VRS3, Table 1). (bottom) Shear rate is ramped up and down, producing repeatable and reversible changes in sample thickness. Boxes highlight individual slow-to-fast velocity ramps (c.f. Figure 6a). External acoustic vibration is applied at ∼4000 s, resulting in logarithmic irreversible compaction, and a qualitative change in the reversible thickness at low velocity (labeled 'dip'). Vibration ceases at ∼10,000 s, after which the low shear-rate compaction returns to the pre-vibration behavior ('no dip').

passband between 1 and 35 kHz, and normalized by the maximum value measured at 100 rad/s. This passband avoids instrument and electronic noise at low frequencies and resonance peaks at higher frequencies (where the amplitude clips). Shear-induced acoustic power increases approximately linearly with shear rate. We will see in a subsequent section that the compaction magnitude also increases linearly with shear rate, indicating a correlation between acoustic power and compaction.

3.5. A Qualitative Model for Shear Zone Thickness

[40] These observations suggest a qualitative model for the steady state thickness of a sheared layer in the presence of acoustic vibration. Both acoustic vibration and shear displacement provide external energy and drive the system to explore packing densities, but in opposite directions and with different timescales. Acoustic vibration produces compaction in the shear zone at a rate that scales with dilation beyond some preferred thickness (perhaps corresponding to random close packing), while shear deformation continually renews contacts and re-dilates the sample at a rate that scales with compaction below some critical state. At some thickness, these two mechanisms are balanced, and a steady state thickness is reached.

[41] These ingredients qualitatively explain the shear-rate dependent behavior seen in the velocity ramps with external vibration (Figure 6). At low shear rates, dilatation is slow, and acoustic compaction has a relatively long time period over which to operate. At somewhat higher shear rates, dilation becomes more rapid, and steady state compaction is reduced, i.e., the thickness versus shear rate curve has a positive slope. At even higher shear rates (i.e., the transitional regime), additional acoustic energy is produced by the shearing itself (Figure 8), driving additional acoustic compaction and producing a negative slope in thickness versus shear rate (Figure 6). This is most pronounced for angular sand grains, which generate high amplitude acoustic vibrations during shear, but is also noticeable for the quieter

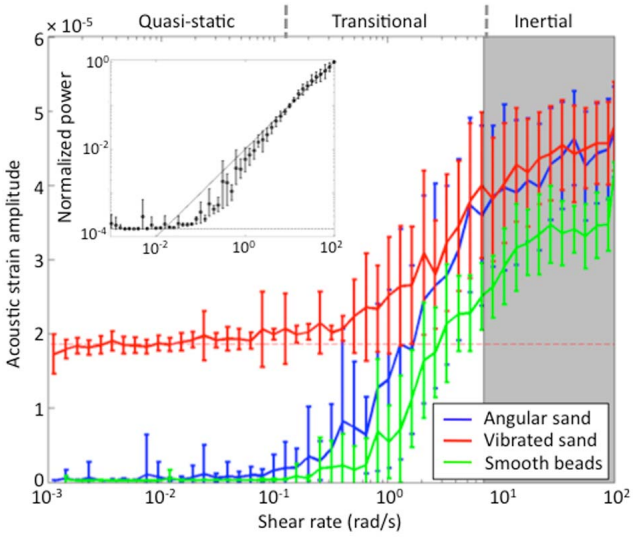

Figure 8. Acoustic vibration amplitude, recorded by an accelerometer attached to the sample jacket. Transitions in steady state thickness (see Figure 6) correspond to transitions in the amplitude of shear-induced vibration. The blue curve is vibration produced by shearing angular sand; the green curve is the vibration produced by glass beads. The red curve shows the superposition of external acoustic vibration on shear-induced vibration produced by angular sand. The accelerometer begins to clip at a shear rate of ∼7 rad/s (gray patch), so the rollover is not entirely physical. At 1 rad/s the shear-induced vibration is equivalent to the external vibration amplitude (dashed red line for reference). Inset: Power of the shear-induced acoustic vibration signal, normalized to the maximum power. Power increases linearly with shear rate (straight line for reference). Error bars show the standard deviation between experimental runs.

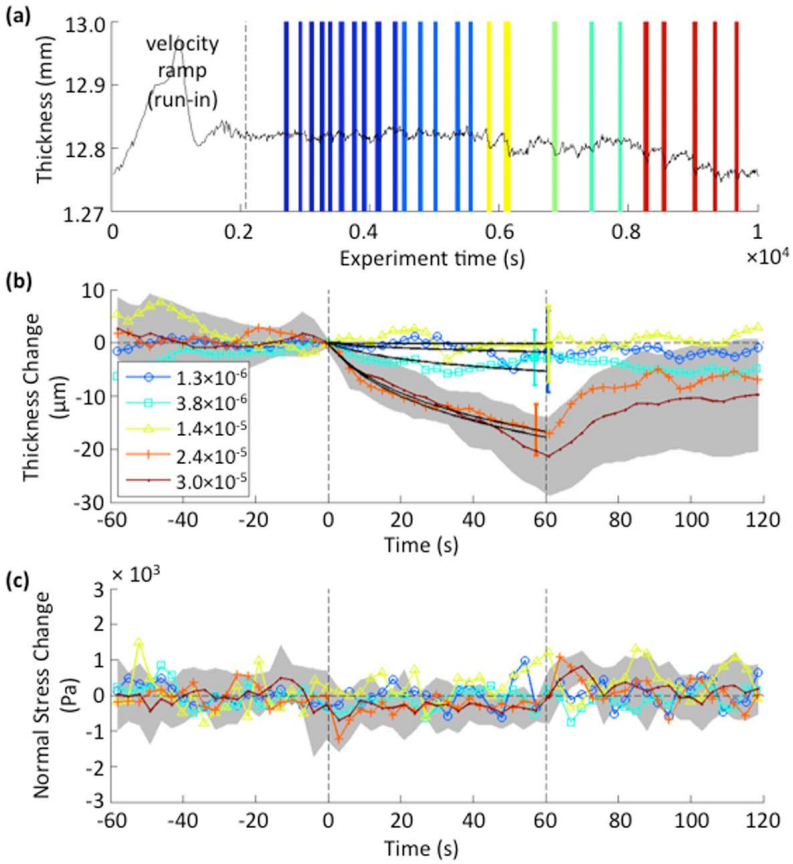

Figure 9. Thickness response of a steadily sheared granular medium subjected to transient acoustic pulses. (a) Thickness versus time for the first 10^4 seconds of the experiment. A velocity ramp is performed to run the sample in over the first 2000 s. The sample is then sheared at 0.01 rad/s and subjected to 60-s acoustic pulses (colored bars, corresponding to amplitude (key in Figure 9b). (b) Stacked thickness response relative to starting thickness for different amplitudes. Black lines are model fits (equation (6)). Grey patch shows one standard deviation between curves in the highest amplitude stack, and are representative of variations in the other stacks. Final thickness variations for the other stacks are shown by error bars at 60 s. (c) stacked normal stress response.

smooth glass beads. Eventually, grain inertial effects dominate the dilatation, the slope of thickness versus shear rate becomes strongly positive, and shear dilatancy and acoustic compaction become irrelevant.

[42] This model also explains the existence of the irreversible component of compaction (e.g., Figure 5). Compaction occurs both in the shear zone and in the slowly or non-deforming bulk far from the shear zone. However, only the compaction that occurs within the shear zone itself can be reversed by shear dilatation.

[43] To develop a more quantitative model of the steady state shear zone thickness, we now investigate the time dependent evolution of thickness in the presence of pulses of externally applied acoustic vibration or internally generated shear-induced vibration. This will constrain the rate of acoustic compaction for a given amplitude vibration. Combined with a measurement of the rate of shear dilatation, a prediction can be made for the steady state thickness as a function of shear rate.

3.6. Acoustic Pulse Experiments

[44] In the externally applied vibration pulse experiments, the angular sand is sheared at a constant 0.01 rad/s and subjected to 60-s bursts of acoustic vibration, after which it is allowed to recover for 3 to 10 min. The bursts are repeated 5–10 times for each acoustic amplitude in order to establish repeatability. The acoustic pulse experiments are summarized in Table 2. The pulses of acoustic vibration produce compaction in the angular sand that increases with the amplitude of the pulse (Figure 9). After cessation of the acoustic burst, the sample recovers a significant component of the thickness that was lost during the acoustic burst, although some of the compaction is irreversible for the highest amplitude pulses. The timescale for re-dilation is greater than 100 s, but is difficult to measure given the natural fluctuations in sample thickness around steady state that occur on this timescale. We interpret the irreversible component of compaction as reflecting incomplete run-in (see Section 3.1).

[45] The evolution of thickness h during the acoustic bursts is fit with a logarithmic function of time t

$$h(t) = h_0 - b\log\left(\frac{t}{\tau^-} + 1\right), \quad (6)$$

where h_0 is the starting thickness, and b and τ^- are empirical constants that describe the magnitude and timescale of compaction, respectively. This function is motivated by other work where the density (i.e., inverse of volume) of a vibrated granular medium is observed to evolve as $\sim 1/\log(t)$ [*Ben-Naim et al.*, 1998; *Caglioti et al.*, 1997; *Knight et al.*, 1995], however other functions (e.g., stretched exponential, double exponential) may fit the data just as well. In this study, we are primarily interested in whether some function that describes the evolution of thickness with time can also predict the steady state observations as a function of shear rate, and a theoretical treatment of the micromechanics of acoustic compaction are beyond the scope of this experimental work.

[46] We could attempt to fit the curves for each vibration amplitude individually, treating both b and τ^- as unknowns. However, there is considerable tradeoff between the two parameters. We choose instead to fix $\tau^- = 10$ s, which produces a good fit to all the curves (including the shear-rate pulse curves in the following section), and fit only the constant b (Table 2). This allows us to map all of the variation with amplitude into a single constant. We justify this choice by noting that while it is possible to fit the curves with a single value of τ^- and varying b, it is not possible to fit the curves with a single value of b and varying τ^-. This implies that the magnitude of compaction is strongly dependent on vibration amplitude, but the timescale is not.

[47] For the highest amplitude vibration, the acoustic compaction produces a very small rapid drop in the normal stress, before the rheometer recovers by lowering the upper plate (Figure 9c). This reflects the fundamental relationship between sample thickness and stress in these experiments (equation (3)). It also shows that the rheometer is unable to keep up with the compaction rate (Appendix B), and the time scale τ^- that we measure in the pulse experiment cannot be taken as a reliable estimate of the intrinsic compaction time scale. We note that the normal stress drop occurs on the timescale of about 1 s. We will eventually solve for the true compaction timescale by fitting a model to the steady state velocity ramp experiments. This effect is relatively negligible for the small-amplitude external vibration experiments, but will be considerably larger for the shear-rate pulses examined in the next section.

[48] The key observations to come out of the acoustic pulse experiments are the logarithmic (or at least, long-tailed) compaction, and the scaling of compaction magnitude parameter b with vibration amplitude.

3.7. Shear Rate Pulses

[49] We now measure compaction during shear rate pulses (Figure 10). We shear the sample at a starting rate of 0.1 rad/s – the maximum shear rate before the transitional weakening – to minimize the direct effect of the velocity jump [*Marone et al.*, 1990; *Marone*, 1991]. We then apply high shear-rate pulses of up to 5 rad/s – the maximum shear rate before inertial dilation effects become apparent in Figure 4. Each curve in Figure 10 represents an average over 5–10 runs (Table 2). The compaction magnitude is observed to increase with the magnitude of the shear rate pulse. When shear rate is stepped back down to 0.1 rad/s, the sample recovers a significant fraction of the shear-induced compaction over a timescale of a hundred seconds, just as it did after the acoustic pulses. We again interpret the additional irreversible component as reflecting incomplete run-in.

[50] We fit the shear-induced compaction curves with the same function as for the acoustic pulses (equation (6)), again with $\tau^- = 10$ s, and again with the caveat that the accuracy of this timescale is limited by the instrument response (Appendix B). The compaction magnitude parameter b is listed in Table 2, along with the amplitude of internal, shear-generated vibration as measured by the accelerometer.

[51] We also fit the thickness evolution in the recovery phase with an exponential function,

$$h(t) = h_0 - \Delta h \exp\left(-\frac{t}{\tau^+}\right), \quad (7)$$

where h_0 is the steady state layer thickness after complete recovery (i.e., the critical thickness for shearing in the absence of vibration), Δh is the total drop during the compaction phase, and τ^+ is the timescale for re-dilation. We find an average recovery timescale τ^+ of 55 s, corresponding to a displacement scale of 5.5 rad, given the shear rate of 0.1 rad/s. We note that this displacement length scale is much longer than the length scale over which strength is recovered after a complete removal of the driving stress, which tends to be on the order of the grain diameter [*Chambon et al.*, 2006; *Toiya et al.*, 2004].

[52] There is strong rapid normal stress drop during the shear-rate jumps due to the slow response of the rheometer (Appendix B), and for the largest amplitudes, the rheometer does not completely catch up to restore the normal force even after 60 s (Figure 10). The underlying compaction timescale, as suggested by the rapid normal stress drop, is therefore likely to be much less than the 10 s estimated from the thickness curves, and may be as little as 1 s or less.

[53] Comparing the values of compaction magnitude versus acoustic strain amplitude for both shear and acoustic pulses (from Table 2), we find that for both pulse types the compaction magnitude is the same for the same amplitude vibration (Figure 11). This indicates that the acoustic compaction mechanism is activated by vibration in the same way regardless of whether the acoustic energy is generated by grain interactions during shear, or injected from an external source. The recovery of dilatation after the cessation of the pulse shows that the acoustic vibration is causing compaction within the actively shearing layer, essentially suppressing shear dilatation and allowing the grains to shear in a more compact configuration at the same stress.

[54] We infer that the compaction observed in the transitional regime during the velocity ramp experiments (Figure 4) is also the result of internally generated acoustic vibration that feeds back on the rheology of the medium. The empirical compaction and dilatation functions that we have measured (equations (6) and (7)) now allow us to formulate a quantitative model for the steady state thickness of a sheared

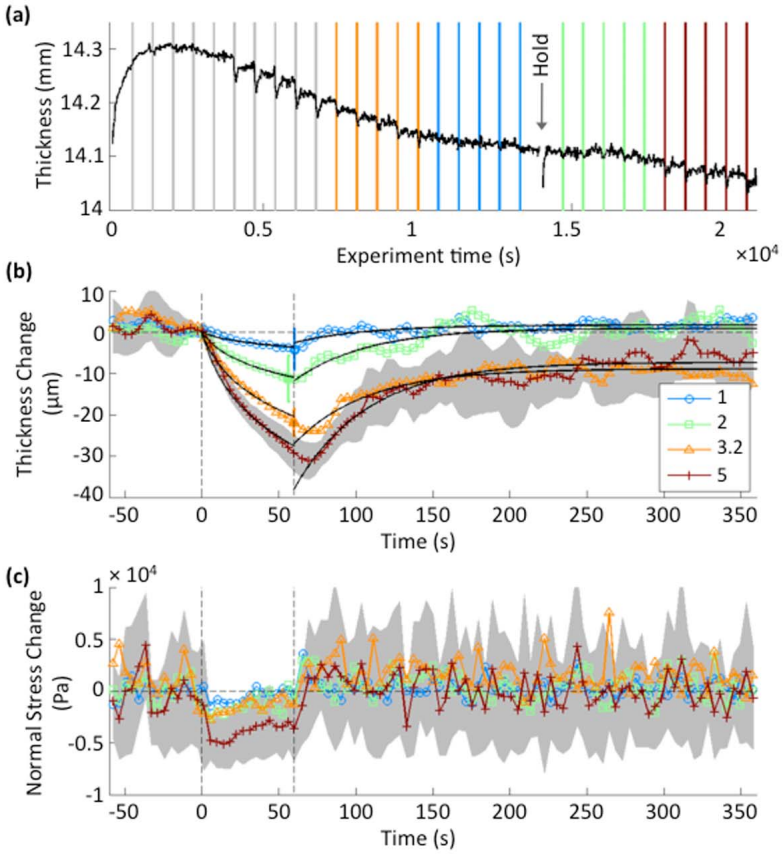

Figure 10. Thickness response of a steadily sheared granular medium subjected to transient shear rate pulses. (a) Thickness versus experimental time. The sample is sheared at 0.1 rad/s, and subjected to 60-s acoustic pulses of higher shear rate (colored bars, corresponding to key in Figure 10b, units: rad/s). 'Hold' marks a point where shear rate and shear stress were transiently set to zero for a few seconds. (b) Stacked thickness response relative to starting thickness for different shear rates. Black lines are model fits (equations (6) and (7)). Grey patch shows one standard deviation between curves for the 5 rad/s stack, and are representative of variations in the other stacks. Final thickness variations for the other stacks are shown by error bars at 60 s. (c) Stacked normal stress response.

layer that reflects the competition between acoustic compaction and shear dilation.

4. Discussion

4.1. Key Components of the Steady State Thickness Model

[55] Any model that explains all the observations presented in Figure 6 must meet at least the following fundamental criteria: 1) At low shear rates, the dilation rate must increase with shear rate in order for external acoustic vibration to produce less steady state compaction at higher velocities. 2) In the transitional regime, the shear-induced acoustic compaction rate must increase faster with shear rate than the shear-induced dilation rate, in order to produce the transitional compaction. 3) The external and internally generated acoustic compaction should behave similarly for equivalent amplitude vibrations.

4.2. A model for the Competition Between Dilatancy and Auto-acoustic Compaction

[56] We propose a simple model for steady state shear zone thickness that invokes a balance between shear dilation and acoustic compaction. The model is based on the empirical curves observed in the vibration pulse experiments, paired with some assumptions to make it consistent with the key components in Section 4.1. The model does not address the physical micro-mechanics of shear dilation and acoustic compaction.

[57] The evolution of shear dilation follows an exponential function of time (equation (7)), as observed in the recovery stage of Figure 10 after the shear-rate pulse. The evolution of acoustic compaction follows a logarithmic function of time (equation (6)). Taking the derivatives of equations (6) and (7) and adding them together gives a total rate of change

$$\frac{dh}{dt} = \frac{(h_0 - h)}{\tau^+} - \frac{b}{\tau^-} \exp\left(-\frac{h_0 - h}{b}\right). \quad (8)$$

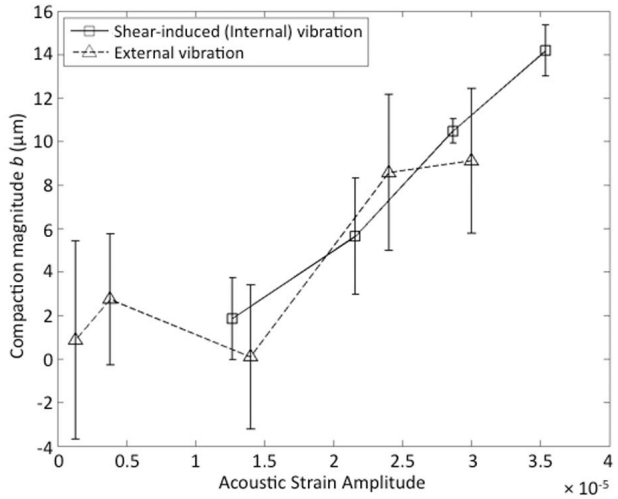

Figure 11. Compaction magnitude b (equation (6)) is a consistent function of acoustic strain amplitude for external (Table 2: Aps1) and internally generated (Table 2: Sps1) acoustic vibration. Compaction magnitude increases linearly above a threshold strain amplitude of about 10^{-5}. Triangles show compaction for external vibration, squares correspond internal, shear-generated vibration, for shear rates of 1, 2, 3.2, and 5 rad/s, from left to right. Each point is an average of 5–10 runs (Table 2), and error bars show standard deviations between runs. The compaction timescale τ^- is fixed to 10 s.

The first term on the right hand side (RHS) is the dilation term, where τ^+ is the timescale for dilation and h_0 is the steady state thickness in the absence of vibration or other perturbations. The second term on the RHS is the compaction term, where τ^- is the timescale for compaction and b is the compaction magnitude, which depends on acoustic vibration amplitude. Equation (8) is expressed in terms of deviations in thickness h. In reality, the dilation rate likely depends on the packing density, normalized to the minimum and maximum packing densities. Since we are unable to measure the packing density directly in the active shear zone of our sample chamber, we make the first-order approximation that changes in thickness dh are proportional to changes in normalized packing density for small deviations from h_0, and formulate the model as a function of thickness only.

[58] We further assume that τ^+ is inversely proportional to the shear rate ω, to be consistent with key component (1) (Section 4.1)

$$\tau^+ = \frac{d}{\omega}, \tag{9}$$

Table 3. Fit Parameters for Steady State Thickness Model (Equation (10))

$b_{acoustic}$[a] (μm)	b_{shear}[a] (μm/rad/s)	d[b] (rad)	τ^{-}[a] (s)
10	18	5.5	1

[a]Fit to combined velocity ramp experiments VRS1–4 (Figure 12).
[b]Fit to acoustic pulse experiment SPS1.

where d is a characteristic angular displacement length scale for renewal of force chains.

[59] For $h < h_0$ the two terms in the RHS of equation (8) drives thickness changes in opposite directions. The steady state thickness of the shear zone is the thickness h at which the dilation rate (equation (8)) = 0, or

$$\frac{h-h_0}{d}\omega = \frac{b}{\tau^-}\exp\left(\frac{h-h_0}{b}\right), \tag{10}$$

where the parameter b depends on the internally and externally generated vibration amplitude. Note that the steady state thickness h is defined only in terms of b and the ratio of the two timescales τ^+/τ^-.

4.3. Experimental Fit

[60] We now return to the steady state thickness (velocity ramp) experiments (Figure 6), and use equation (10) to solve for b as a function of shear rate. We use the same equation to solve separately for b in the case with and without external vibration, and refer to the fit parameters as $b_{acoustic}$ and b_{shear}, respectively (Table 3).

[61] We fit the acoustic compaction magnitude parameter $b_{acoustic}$ (equation (10)) over the low-velocity range, where shear-induced compaction is negligible (Figure 12). Since the compaction timescale in the pulse experiments is unreliable (Appendix B), we also fit τ^- setting the dilatation recovery length scale d to 5.5 radians, as estimated from the shear-rate pulse experiments. This gives a compaction timescale τ^-=1 s, consistent with the timescale for the large

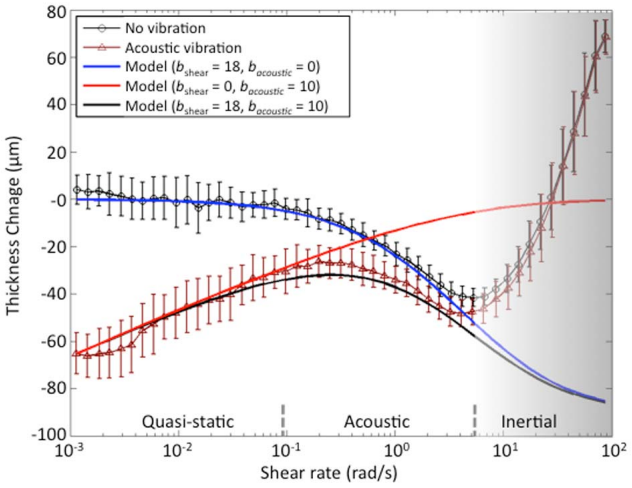

Figure 12. Observed and modeled steady state thickness of the shear zone h as a function of shear rate ω (equation (10)). Observations (with error bars) are the same as in Figure 6a for angular sand under shear-induced and external acoustic vibration. The red curve is the modeled contribution from external vibration only; the blue curve is the modeled contribution from shear-induced vibration; and the black curve shows the modeled sum of the two compaction components. Compaction magnitude parameters are given in the legend. Other parameters are τ^- = 1 s, dilatation length scale d = 5.5 rad (Table 3), and starting thickness h_0 = 0. The increase in thickness for both curves at high shear rates is caused by inertial dilation and is not addressed by the model.

drop in normal force in acoustic pulse experiments, and a value of $b_{\text{acoustic}} = 10$ μm, consistent with the compaction magnitude from the acoustic pulse experiment using the same amplitude external vibration (3×10^{-5}) (Table 2).

[62] The shear-rate dependent steady state layer thickness at low shear rate is explained quite well by a constant compaction magnitude b_{acoustic} (Figure 12). The systematic relationship between steady state thickness and shear rate simply reflects the longer timescale for shear dilation at low shear rates (equation (9)). At low shear rates, the acoustic compaction has a relatively long time to operate. As the shear rate increases, less and less compaction can occur within the timescale for dilation.

[63] We fit the shear-induced compaction component b_{shear} with a linear function of shear rate (Figure 12), motivated by the linear increase in shear-induced acoustic power (Figure 7, inset). We fix τ^- to 1 s, as found for the external acoustic vibration component at low shear rates. A good fit is obtained with a shear-induced compaction magnitude $b_{\text{shear}} = 18$ μm/(rad/s). A possible interpretation of the linear increase with shear rate would be that each discrete acoustic emission (AE) has a statistically constant amplitude, independent of shear rate, and the rate of AE increases proportional to shear rate. This may imply that AE are produced by an elastic process, such as force chain buckling, as opposed to a collisional process, which should scale as shear rate squared.

[64] The steady state compaction in the presence of both shear-induced and external acoustic compaction is very nearly predicted by a linear sum between the acoustic and shear-induced compaction components (Figure 12):

$$b_{total} = b_{acoustic} + \omega b_{shear}. \tag{11}$$

We conclude that the mechanism for acoustic compaction of the actively shearing layer is identical, regardless of whether the vibration is generated internally or externally, and the compaction in the transitional regime is a result of internally generated vibration.

4.4. The Quasi-static–Acoustic Transition: A New Granular Flow Regime

[65] In Section 1 we introduced the inertial transition in terms of a balance between inertial dispersive pressure and normal stress (equations (1) and (2)). We now discuss the intermediate-rate flow behavior in terms of a new "acoustic" flow regime, where the acoustic pressure balances the normal stress.

[66] The transition to the acoustic regime is observed at shear rates as low as 0.1 rad/s (0.95) mm/s. The inertial dispersive pressure at this velocity is $<10^{-6}$ times the confining pressure, and the change in rheology cannot readily be attributed to the inertial transition. Instead, this low-velocity transition represents the transition to acoustic fluidization. The acoustic pressure p_a equals the bulk modulus ($K = \rho c^2$) times the acoustic strain ε, giving

$$P_a = \rho c^2 \varepsilon, \tag{12}$$

where ρ is the density of the medium, c is the acoustic wave speed [*Thompson*, 1971, chap. 4]. We experimentally identify acoustic compaction at a threshold strain ε on the order of 10^{-5} (Figures 9 and 11). Taking the acoustic velocity $c \sim 500$ m/s, and $\rho = 2000$ kg/m^3, the threshold acoustic pressure (equation (12)) is 5 kPa, which is on the order of the confining stress (7 kPa). This suggests another non-dimensional number, similar to the inertial number (equation (2))

$$J \equiv \frac{\rho c^2 \varepsilon}{p}. \tag{13}$$

The transition from the quasi-static to acoustic granular flow regime occurs when confining pressure p is balanced by acoustic pressure, i.e., $J = 1$. Note that the acoustic approximation becomes invalid as the acoustic pressure fluctuations approach the absolute pressure, i.e., $J \sim 1$, and the acoustic wave speed should decrease dramatically in the fluidized regime, limiting further increases in the acoustic pressure.

[67] *Melosh* [1979, 1996] suggested that acoustic fluidization could allow granular materials to flow at shear stresses far below the frictional strength suggested by the overburden pressure. In this theory, acoustic pressure fluctuations produce transient reductions of the normal stress, allowing stress to locally exceed the Coulomb frictional threshold. The mechanism is activated when the peaks in acoustic pressure reach the order of the overburden. The energy density to "fluidize" a rock mass by acoustic vibration is orders of magnitude smaller than the energy density required to fluidize the same rock mass by kinetic particle motion [*Melosh*, 1979]. There is some experimental evidence for the importance of acoustic resonances in mobilizing a granular medium at vibration amplitudes much smaller than required to balance gravitational acceleration [*Umbanhowar and van Hecke*, 2005].

[68] The mechanism we propose here is very similar to the acoustic fluidization of *Melosh* [1979], but differs in two fundamental ways. First, instead of normal force being reduced directly by acoustic stress fluctuations, it is reduced indirectly through the phenomenon of acoustic compaction. The general conceptual model for acoustic compaction comes out of granular physics [*Mehta*, 2007]. In this framework, shear stress in a granular packing is supported by a framework of force chains, supported by a network of buttressing grains [*Majmudar and Behringer*, 2005]. Increased loading in the shear direction primarily compresses and rotates the strong force chains, which leads to bulk dilatation [*Tordesillas et al.*, 2011]. Particle reconfiguration (compaction) can only occur when strongly loaded force chains buckle catastrophically. When static equilibrium is restored by the formation of new force chains, the packing is again in a jammed state and unable to explore configurations. Acoustic vibration, on the other hand, accesses both strong force chain grains and buttressing grains directly, and may continuously disrupt grain contacts without catastrophic buckling of force chains. This promotes incremental compaction into a lower energy configuration.

[69] The second fundamental distinction between our model and the model of *Melosh* [1979] is that the acoustic energy is continuously produced within the shear zone through the interactions of angular particles. The auto-acoustic fluidization mechanism does not therefore require that the fault zone capture and scatter radiated seismic waves.

[70] Auto-acoustic fluidization, as observed in these experiments, is related to the amplitude of acoustic vibration produced through grain interactions during shear. As such, it is strongly dependent on the characteristics of the grains. Angular grains generate sufficient acoustic energy to strongly affect the rheology of the flow, but smooth glass beads do not. This implies that the physical characteristics of gouge particles observed in fault zones can tell us something about the rheology of the flow during rupture.

[71] For this mechanism to be active at seismogenic depths of ~10 km, with overburden pressure on the order of 3×10^8 Pa, assuming $c = 3 \times 10^3$ m/s, and $\rho = 3 \times 10^3$ kg/m^3, equation (13) requires that the acoustic strain amplitude ε be on the order of 10^{-2}. It is not known how internally generated acoustic strain amplitude should scale with slip rate at these conditions, and this value is at the upper limit of plausible elastic strain in rock and well into the nonlinear elastic regime, where other mechanisms may dominate the rheology [*Johnson and Jia*, 2005]. However, if the effective confining pressure is reduced by fluid pressure or some other mechanism, the required acoustic strain amplitude will be reduced accordingly. There is considerable evidence supporting the idea that effective pressures may indeed be low in many faults [*Hickman et al.*, 1995; *Sleep and Blanpied*, 1992].

4.5. The Acoustic–Inertial Transition

[72] The acoustic transition described above defines the point at which the active shear zone begins to compact relative to the quasi-static thickness. This compaction grows larger with shear rate until the inertial regime is entered. Following the same recipe as for equations (1) and (13), we define the acoustic-inertial transition as the point at which the dispersive pressure of granular collisions exceeds the acoustic pressure, introducing a third non-dimensional number

$$K \equiv \frac{\rho v^2}{\rho c^2 \varepsilon} = \frac{I}{J}. \tag{14}$$

The acoustic number J is limited to 1, however, because the acoustic pressure is bounded by the confining pressure. In the acoustic regime, therefore, the non-dimensional number K therefore reduces to the inertial number I. This means that the inertial transition occurs at the same shear rate regardless of whether the transition is from the acoustic or the quasi-static flow regimes. However, the transition from acoustic to dilatational inertial flow begins at a reduced shear zone thickness with respect to the quasi-static regime (i.e., out of the dip in Figure 4).

4.6. Future Directions

[73] These experiments were carried out at very low confining stresses (7 kPa) and with relatively high porosity in order to isolate deformation by grain rolling, sliding, and force chain reorganization, rather than cataclasis. The low confining stress is also required in order to approach the inertial granular flow regime in our experimental apparatus. This means that elastic deformation of individual grains is relatively small, fragmentation is rare, and there is little contribution to the strength of the material from fine powder in the interstices between large grains. This may not constitute a perfect analogy with deformation in natural fault gouge and other geophysical flows, however by isolating the mechanisms contributing to porosity creation and reduction at low confining stresses, we can improve our understanding of more complicated systems, including those involving cataclasis. The auto-acoustic compaction mechanism described here should operate in noisy granular flows as long as there is nonzero porosity during shear.

[74] Future experiments must: 1) establish what range of grain characteristics (angularity, aspect ratio, etc.) are capable of generating sufficient acoustic vibration to feed back on the rheology of the shear flow; 2) quantify how the amplitude of acoustic vibration scales with shear rate at seismically relevant confining stresses, as well as under constant volume conditions; and 3) establish the relative importance of acoustic compaction when a range of micromechanical processes are active, including cataclasis, thermal pressurization, and dilatational hardening. On the acoustic compaction side, experiments should explore a range of acoustic pulse amplitudes, frequencies, and durations, with a variety of particle shape and size distributions.

[75] The auto-acoustic compaction model we have proposed in Section 4.2 is semi-empirical, and therefore may not be the only possible description of the thickness changes under shear and vibration. A physical model that is tied to the micromechanical processes of dilation and compaction is called for. It will be particularly important to understand what processes set the timescales for acoustic compaction and the recovery of dilation under shear.

5. Conclusion

[76] We have experimentally measured the thickness of a granular shear flow over a range of geophysically relevant shear rates. We have quantified the physical conditions for a new granular flow regime at shear rates transitional between quasi-static and inertial granular flow, that we term the acoustic regime. In this regime, internally generated vibrations induce auto-acoustic compaction of the dilated shear zone. The steady state thickness of the shear zone is described by a semi-empirical model that balances auto-acoustic compaction and shear dilatation.

[77] Experiments using external acoustic vibration reveal the fundamental link between the intermediate shear-rate compaction and acoustic compaction, showing that the same magnitude of steady state compaction is achieved for the same magnitude of acoustic vibration, regardless of whether it is applied externally or generated internally by shearing and grain collisions. The magnitude of internally generated acoustic vibration is dependent on the characteristics of the grains, and thus the phenomenon of auto-acoustic fludization occurs for angular grains, but not for quieter smooth grains.

[78] The acoustic regime is activated when peak acoustic pressure from shear-induced vibration exceeds the confining stress. At 10 kPa confining stress, this transition occurs at a shear rate of only 1 mm/s in angular sand – four orders of magnitude below shear rates typical of the transition to inertial, dispersive granular flow.

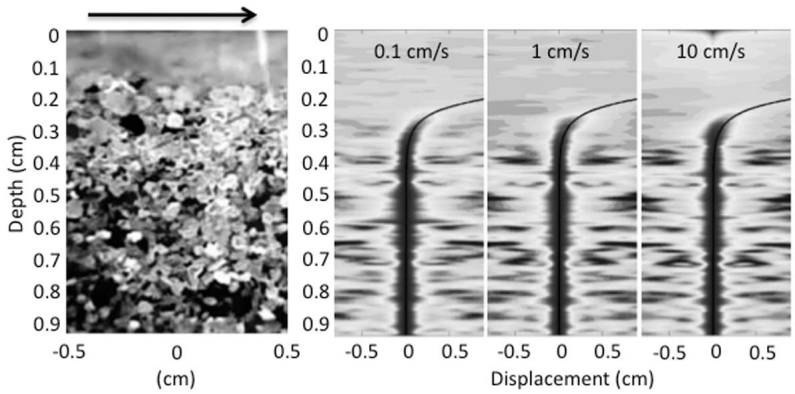

Figure A1. Displacement profiles for different velocities. The left panel shows a snapshot of the angular sand, which is being sheared to the right. The following panels show horizontal cross-correlation of snapshots taken at a constant displacement (10 cm) but for different shear rates (0.1, 1, and rad/s from left to right). The darker colors reflect higher cross correlation coefficients. Grain rotation and non-horizontal particle motion prevent correlation beyond a few mm displacement. An exponential function (black curve) is fit to the first cross-correlation image (0.1 cm/s) and superposed on the adjacent panels. The shear-rate profile does not change except through a multiplicative pre-factor.

[79] Earthquake slip produces high frequency shaking both in the wake and in advance of a propagating rupture front. While the experimental conditions in this study are far from the conditions of fault zones, scaling the acoustic fluidization process up to seismogenic conditions suggests that this mechanism may be an important velocity weakening mechanism if confining stresses during earthquake rupture are sub-lithostatic.

Appendix A: Shear Zone Thickness

[80] The shear zone in each experiment is restricted to a thin layer near the upper rotor, with displacement and shear rate decreasing rapidly with distance from the rotor. The exponential displacement profile is constant regardless of the shear rate, that is, the velocity profile changes only through a pre-factor proportional to the rotor velocity (Figure A1).

[81] We image the active shear zone by cross-correlating video snapshots of the outer boundary using a high-definition webcam. Snapshots are taken at rim displacement intervals of 10 cm for three representative velocities: 0.1, 1, and 10 cm/s. We then cross-correlate successive images to estimate horizontal lag as a function of depth. This involves taking a horizontal row of pixels from each pair of images and calculating the cross correlation function between the two. The lag corresponding to the maximum in the correlation function is taken as the horizontal displacement. We repeat this process for each row of pixels to get displacement as a function of depth away from the rotor. We then average the cross correlation function over 100 image pairs to produce the images in Figure A1.

[82] The shear rate profile with depth is well fit by an exponential function with a decay length scale of 0.63 mm, or approximately 2 grain diameters (Figure A1). We fit an exponential function to the peaks in the cross-correlation image for the shear rate of 0.1 cm/s, and then superpose this fit to the second two cross correlation images. No adjustment in the fit parameters is required to fit the profile at 1 cm/s and 10 cm/s. This is consistent with the results of *Lu et al.* [2007].

Appendix B: Rheometer Response to a Sudden Pressure Drop

[83] The AR2000ex rheometer maintains normal pressure through a firmware feedback loop, adjusting the height of the rotor (gap) until the measured force falls within the bounds set by the controller software. The algorithm for adjusting the gap in response to a sudden drop in normal stress is not documented in the rheometer software, and thus the instrument response time after a sudden compaction event is unknown. We perform a simple experiment in which we observe the rheometer response to a sudden compaction event (drop in pressure).

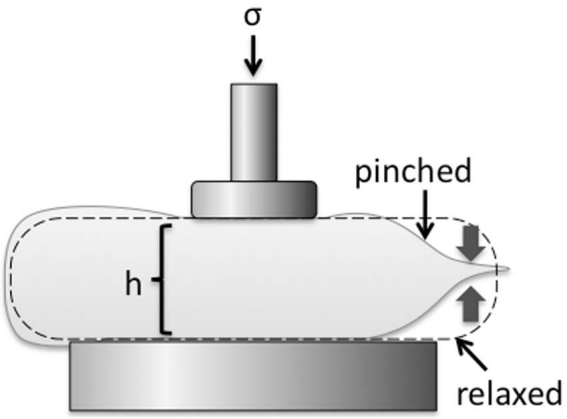

Figure B1. Cartoon of experimental setup. The rheometer rotor is lowered into contact with an inflated plastic bag, which is pinched on the edge to increase the pressure. At the start of the experiment, the bag is released, resulting in a sudden relaxation in pressure (dashed outline).

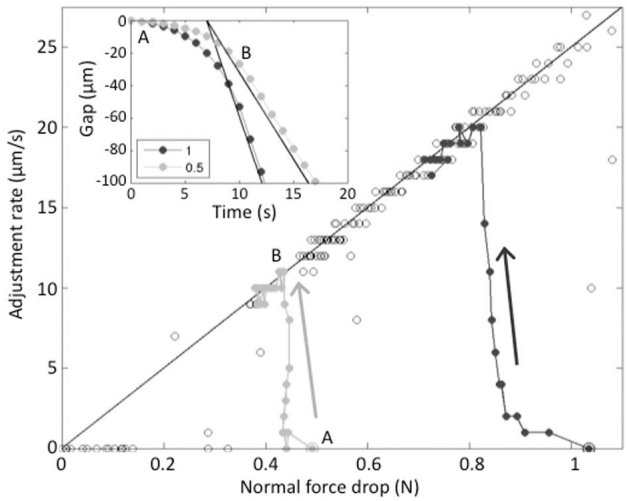

Figure B2. Gap adjustment rate as a function of the reduction in normal force. Open circles show the response to continuous fluctuations in the resisting force. The maximum adjustment rate depends linearly on the deviation of normal force from the nominal value (25 μm/s/N), and the adjustment begins immediately. Filled circles show paths for the case of a sudden force drop, where the normal force is reduced from 1 N to 0.5 N (gray) or 0 N (black). For these sudden drops, there is a delayed rheometer response, during which the gap adjustment rate accelerates from zero (large circles at start of path) to the maximum rate over ~10 s. Inset: Paths for sudden force drop experiments as a function of time, showing the ~10 s delay. The maximum rates are shown by straight lines for reference. Points A and B on the inset corresponds to points A and B along the path in the main figure.

[84] The experiment proceeds as follows: we place an air bladder (1 qt. Ziploc-style bag) on the rheometer platform (Figure B1). A corner of the bag is pinched to reduce the internal volume and increase the pressure. The rotor is then lowered until it compresses the bag and a normal force of 1 N is registered by the rheometer. Finally, the constriction on the bag is then suddenly released, resulting in a rapid drop in pressure. We then observe the change in gap (rotor height) with time (Figure B2, inset). The experiment is repeated for pressure drops of ~0.5 and ~1 N, as well as for continuous pressure fluctuations induced by intermittently squeezing and releasing the bag.

[85] We find that while the rheometer responds continuously to continuous pressure fluctuations, it has a significantly delayed response to a sudden pressure drop. The gap decreases gradually at first, before accelerating over ~10 s, up to a maximum adjustment rate that is dependent on the deviation of the normal force from the nominal value (25 μm/s/N) (Figure B2). This response explains the prolonged drop in normal force in experiment SPS1 (Figure 10), and means that the measured timescale for compaction in Section 3.6 (Experiments SPS1 and APS1) must be treated as an upper bound on the intrinsic compaction timescale.

[86] **Acknowledgments.** N. van der Elst and E. E. Brodsky were supported by a grant from institutional support at Los Alamos National Lab via the Institute of Geophysics and Planetary Physics. P. Johnson and P.-Y. Le Bas were supported by institutional support via the LDRD office at Los Alamos. We are indebted to our anonymous reviewers for very thorough and constructive reviews that have improved the clarity and organization of this article.

References

Aharonov, E., and D. Sparks (1999), Rigidity phase transition in granular packings, *Phys. Rev. E*, *60*(6), 6890–6896, doi:10.1103/PhysRevE.60.6890.

Bagnold, R. A. (1954), Experiments on a gravity-free dispersion of large solid spheres in a Newtonian fluid under shear, *Proc. R. Soc. A*, *225*(1160), 49–63.

Beeler, N. M., T. E. Tullis, M. L. Blanpied, and J. D. Weeks (1996), Frictional behavior of large displacement experimental faults, *J. Geophys. Res.*, *101*(B4), 8697–8715, doi:10.1029/96JB00411.

Ben-Naim, E., J. B. Knight, E. R. Nowak, H. M. Jaeger, and S. R. Nagel (1998), Slow relaxation in granular compaction, *Physica D*, *123*(1–4), 380–385, doi:10.1016/S0167-2789(98)00136-5.

Biegel, R. L., C. G. Sammis, and J. H. Dieterich (1989), The frictional-properties of a simulated gouge having a fractal particle distribution, *J. Struct. Geol.*, *11*(7), 827–846, doi:10.1016/0191-8141(89)90101-6.

Bocquet, L., W. Losert, D. Schalk, T. C. Lubensky, and J. P. Gollub (2001), Granular shear flow dynamics and forces: Experiment and continuum theory, *Phys. Rev. E*, *65*(1), 011307, doi:10.1103/PhysRevE.65.011307.

Caglioti, E., V. Loreto, H. J. Herrmann, and M. Nicodemi (1997), A "tetris-like" model for the compaction of dry granular media, *Phys. Rev. Lett.*, *79*(8), 1575–1578, doi:10.1103/PhysRevLett.79.1575.

Campbell, C. S. (1990), Rapid granular flows, *Annu. Rev. Fluid Mech.*, *22*, 57–90, doi:10.1146/annurev.fl.22.010190.000421.

Campbell, C. S. (2005), Stress-controlled elastic granular shear flows, *J. Fluid Mech.*, *539*, 273–297, doi:10.1017/S0022112005005616.

Campbell, C. S. (2006), Granular material flows: An overview, *Powder Technol.*, *162*(3), 208–229, doi:10.1016/j.powtec.2005.12.008.

Cates, M. E., J. P. Wittmer, J. P. Bouchaud, and P. Claudin (1998), Jamming, force chains, and fragile matter, *Phys. Rev. Lett.*, *81*(9), 1841–1844, doi:10.1103/PhysRevLett.81.1841.

Chambon, G., J. Schmittbuhl, and A. Corfdir (2006), Frictional response of a thick gouge sample: 1. Mechanical measurements and microstructures, *J. Geophys. Res.*, *111*, B09308, doi:10.1029/2003JB002731.

Clement, E. (1999), Rheology of granular media, *Curr. Opin. Colloid Interface Sci.*, *4*, 294–299, doi:10.1016/S1359-0294(99)90004-3.

Coghill, P. J., and P. Giang (2011), Ultrasonic velocity measurements in powders and their relationship to strength in particles formed by agglomeration, *Powder Technol.*, *208*(3), 694–701, doi:10.1016/j.powtec.2010.11.040.

da Cruz, F., S. Emam, M. Prochnow, J. N. Roux, and F. Chevoir (2005), Rheophysics of dense granular materials: Discrete simulation of plane shear flows, *Phys. Rev. E.*, *72*(2), 021309, doi:10.1103/PhysRevE.72.021309.

Daniels, K. E., and R. P. Behringer (2005), Hysteresis and competition between disorder and crystallization in sheared and vibrated granular flow, *Phys. Rev. Lett.*, *94*(16), 168001, doi:10.1103/PhysRevLett.94.168001.

Dijksman, J. A., G. H. Wortel, L. T. H. van Dellen, O. Dachot, and M. van Hecke (2011), Jamming, yielding and rheology of weakly vibrated granular media, *Phys. Rev. Lett.*, *107*(10), 108303, doi:10.1103/PhysRevLett.107.108303.

GDR MiDi (2004), On dense granular flows, *Eur. Phys. J. E*, *14*, 341–365, doi:10.1140/epje/i2003-10153-0.

Hickman, S., R. Sibson, and R. Bruhn (1995), Introduction to special section: Mechanical involvement of fluids in faulting, *J. Geophys. Res.*, *100*(B7), 12,831–12,840, doi:10.1029/95JB01121.

Hutton, C. O. (1959), Mineralogy of beach sands between Halfmoon and Monterey bays, California, *Rep., 59*, Calif. Div. of Mines, Sacramento.

Iverson, R. M. (1997), The physics of debris flows, *Rev. Geophys.*, *35*(3), 245–296, doi:10.1029/97RG00426.

Jaeger, H. M., S. R. Nagel, and R. P. Behringer (1996), Granular solids, liquids, and gases, *Rev. Mod. Phys.*, *68*(4), 1259–1273, doi:10.1103/RevModPhys.68.1259.

Jia, X., C. Caroli, and B. Velicky (1999), Ultrasound propagation in externally stressed granular media, *Phys. Rev. Lett.*, *82*(9), 1863–1866, doi:10.1103/PhysRevLett.82.1863.

Johnson, P. A., and X. Jia (2005), Nonlinear dynamics, granular media and dynamic earthquake triggering, *Nature*, *437*(7060), 871–874, doi:10.1038/nature04015.

Johnson, P. A., H. Savage, M. Knuth, J. Gomberg, and C. Marone (2008), Effects of acoustic waves on stick–slip in granular media and implications for earthquakes, *Nature*, *451*(7174), 57–60, doi:10.1038/nature06440.

Johnson, P. A., B. M. Carpenter, M. Knuth, B. M. Kaproth, P.-Y. Le Bas, E. G. Daub, and C. Marone (2012), Nonlinear dynamical triggering of slow-slip on simulated earthquake faults, *J. Geophys. Res.*, *117*, B04310, doi:10.1029/2011JB008594.

Knight, J. B., C. G. Fandrich, C. N. Lau, H. M. Jaeger, and S. R. Nagel (1995), Density relaxation in a vibrated granular material, *Phys. Rev. E*, *51*(5), 3957–3963, doi:10.1103/PhysRevE.51.3957.

Kuwano, O., and H. Takahiro (2011), Flash weakening is limited by granular dynamics, *Geophys. Res. Lett.*, *38*, L17305, doi:10.1029/2011GL048530.

Liu, A. J., and S. R. Nagel (1998), Nonlinear dynamics: Jamming is not just cool any more, *Nature*, *396*(6706), 21–22, doi:10.1038/23819.

Liu, A. J., and S. R. Nagel (2010), The jamming transition and the marginally jammed solid, *Annu. Rev. Condens. Matter Phys.*, *1*(1), 347–369, doi:10.1146/annurev-conmatphys-070909-104045.

Lu, K., E. E. Brodsky, and H. P. Kavehpour (2007), Shear-weakening of the transitional regime for granular flow, *J. Fluid Mech.*, *587*, 347–372, doi:10.1017/S0022112007007331.

Lu, K., E. E. Brodsky, and H. P. Kavehpour (2008), A thermodynamic unification of jamming, *Nat. Phys.*, *4*(5), 404–407, doi:10.1038/nphys934.

Majmudar, T. S., and R. P. Behringer (2005), Contact force measurements and stress-induced anisotropy in granular materials, *Nature*, *435*(7045), 1079–1082, doi:10.1038/nature03805.

Makse, H. A., N. Gland, D. L. Johnson, and L. Schwartz (2004), Granular packings: Nonlinear elasticity, sound propagation, and collective relaxation dynamics, *Phys. Rev. E*, *70*(6), 061302, doi:10.1103/PhysRevE.70.061302.

Marone, C. (1991), A note on the stress-dilatancy relation for simulated fault gouge, *Pure Appl. Geophys.*, *137*(4), 409–419, doi:10.1007/BF00879042.

Marone, C., C. B. Raleigh, and C. H. Scholz (1990), Frictional behavior and constitutive modeling of simulated fault gouge, *J. Geophys. Res.*, *95*(B5), 7007–7025, doi:10.1029/JB095iB05p07007.

Mehta, A. (Ed.) (2007), *Granular Physics*, Cambridge Univ. Press, Cambridge, U. K., doi:10.1017/CBO9780511535314.

Melosh, H. J. (1979), Acoustic fluidization: New geologic process, *J. Geophys. Res.*, *84*(B13), 7513–7520.

Melosh, H. J. (1996), Dynamical weakening of faults by acoustic fluidization, *Nature*, *379*(6566), 601–606, doi:10.1038/379601a0.

Nowak, E. R., J. B. Knight, M. L. Povinelli, H. M. Jaeger, and S. R. Nagel (1997), Reversibility and irreversibility in the packing of vibrated granular material, *Powder Technol.*, *94*(1), 79–83, doi:10.1016/S0032-5910(97)03291-9.

Paull, C. K., P. Mitts, W. Ussler, R. Keaten, and H. G. Greene (2005), Trail of sand in upper Monterey Canyon: Offshore California, *Geol. Soc. Am. Bull.*, *117*(9), 1134–1145, doi:10.1130/B25390.1.

Reynolds, O. (1885), On the dilatancy of media composed of rigid particles in contact, *Philos. Mag.*, *20*, 469–481.

Savage, S. B. (1984), The mechanics of rapid granular flows, *Adv. Appl. Mech.*, *24*, 289–366, doi:10.1016/S0065-2156(08)70047-4.

Sleep, N. H., and M. L. Blanpied (1992), Creep, compaction and the weak rheology of major faults, *Nature*, *359*(6397), 687–692, doi:10.1038/359687a0.

Thompson, P. A. (1971), *Compressible-Fluid Dynamics*, McGraw-Hill, New York.

Toiya, M., J. Stambaugh, and W. Losert (2004), Transient and oscillatory granular shear flow, *Phys. Rev. Lett.*, *93*(8), 088001, doi:10.1103/PhysRevLett.93.088001.

Tordesillas, A., J. Y. Shi, and T. Tshaikiwsky (2011), Stress-dilatancy and force chain evolution, *Int. J. Numer. Anal. Methods Geomech.*, *35*(2), 264–292, doi:10.1002/nag.910.

Umbanhowar, P., and M. van Hecke (2005), Force dynamics in weakly vibrated granular packings, *Phys. Rev. E*, *72*(3), 030301, doi:10.1103/PhysRevE.72.030301.

Veje, C. T., D. W. Howell, and R. P. Behringer (1999), Kinematics of a two-dimensional granular Couette experiment at the transition to shearing, *Phys. Rev. E*, *59*(1), 739–745, doi:10.1103/PhysRevE.59.739.

Walton, K. (1987), The effective elastic-moduli of a random packing of spheres, *J. Mech. Phys. Solids*, *35*(2), 213–226, doi:10.1016/0022-5096(87)90036-6.